



Novel high surface area stainless steel wire mesh supported $\text{Ni}_{0.7}\text{Zn}_{0.3}\text{O}$ solid solution prepared by room temperature sacrificial template accelerated hydrolysis. Application in the production of hydrogen from methanol

Tan Thi Vu, Teresa Valdés-Solís, Gregorio Marbán*

Instituto Nacional del Carbón (INCAR-CSIC), Chemistry of Materials, c/Francisco Pintado Fe 26, 33011 Oviedo, Spain

ARTICLE INFO

Article history:

Received 7 March 2014

Received in revised form 25 April 2014

Accepted 3 May 2014

Available online 10 May 2014

Keywords:

ZnO

$\text{Ni}_{0.7}\text{Zn}_{0.3}\text{O}$

Sacrificial template

Methanol steam reforming

Methanol decomposition

ABSTRACT

This work describes for the first time the room-temperature synthesis of a high surface area $\text{Ni}_{0.7}\text{Zn}_{0.3}\text{O}$ solid solution by sacrificial template accelerated hydrolysis. The synthesis employs a highly polar ZnO template supported on the surface of a stainless steel wire mesh (SSWM) that allows the material to be produced in a monolithic configuration. The resulting material has a large surface area of around $100\text{ m}^2\text{ g}^{-1}$ and is obtained in a yield of up to 40 wt.% on the SSWM in the synthesis conditions employed in this work. Characterization of the material by TPR, XRD and XPS revealed that the solid solution is composed of an oxygen-defective bulk and a partially oxidized surface. As part of this study, the $\text{Ni}_{0.7}\text{Zn}_{0.3}\text{O}$ solid solution has been tested for the first time as a catalyst, displaying high activity in both the methanol steam reforming and the methanol decomposition reactions. At temperatures below 400°C the catalyst is not very selective in the methanol steam reforming reaction, and produces large amounts of CO. However, at more elevated temperatures the water gas shift reaction improves the hydrogen yield and the carbon selectivity towards CO_2 , especially over higher contact times. Despite some catalyst deactivation due to coke deposition, methanol decomposition occurs with high conversion degrees and hydrogen yields in the temperature range of $250\text{--}350^\circ\text{C}$.

© 2014 Elsevier B.V. All rights reserved.

1. Introduction

Nowadays the number of catalysts being designed and developed by research groups at public institutions and private companies is so high that it is becoming more and more difficult to find new active formulae that have never been tested before in a catalytic process. What is more, the simpler the chemical formulation of the catalyst is (mono or bimetallic oxides), the harder the task. One of the formulations that has not yet been tested is the solid solution $\text{Ni}_{0.7}\text{Zn}_{0.3}\text{O}$. The ability of zinc to dissolve in the NiO rocksalt lattice was recognized long ago [1,2]. ZnO has a propensity to lose surface oxygen when heated in air, leaving excess zinc atoms behind that diffuse into interstitial positions of the lattice in order to preserve the electrostatic balance [2]. Conversely, when heated in air NiO takes up excess oxygen, as a result of which cation vacancies appear by the migration of nickel ions to the surface [2]. When both oxides are heated together, these complementary

trends explain why zinc atoms dissolve into the NiO crystal. The solubility limit below which the rocksalt crystal structure of NiO is preserved lies in the range 0.3–0.4 (Zn/(Zn + Ni) molar ratio) [1,2]. For higher fractions of zinc the wurtzite structure of ZnO appears on the XRD plots [3]. Auger parameter analysis indicates that the zinc has the octahedral coordination typical of a rocksalt structure [3]. This coordination is unusual for Zn^{2+} , which prefers a tetrahedral coordination, as in the wurtzite structure of ZnO. The presence of Zn in the crystal lattice of NiO can be expected to affect its magnetic and electronic properties. NiO is antiferromagnetic and the interstitial presence of Zn atoms provokes a decrease in the Néel temperature, from 523 K (NiO) to 312 K ($\text{Ni}_{0.7}\text{Zn}_{0.3}\text{O}$) [4]. Similarly, the catalytic properties of $\text{Ni}_{0.7}\text{Zn}_{0.3}\text{O}$ might also be expected to differ from those of NiO.

In line with this reasoning it seems clear that $\text{Ni}_{0.7}\text{Zn}_{0.3}\text{O}$ must be prepared through a thermal process under air in order to create the necessary vacancies to provoke the migration of zinc cations towards the crystal structure of NiO (pulsed laser deposition also allows films of $\text{Ni}_{0.7}\text{Zn}_{0.3}\text{O}$ to be grown [5]). A temperature of at least 500°C is thought to be required for the incorporation of zinc into the rocksalt structure of NiO [6]. This specificity is a drawback

* Corresponding author. Tel.: +34 985119090; fax: +34 985297662.
E-mail address: greca@incar.csic.es (G. Marbán).

for the synthesis of materials with a high surface area, a property that is generally desired when designing catalysts, and may explain why this material has never been tested as a catalyst. CVD [7], solvothermal alcoholysis [8,9] or co-precipitation [10] allows the formation of nickel-doped ZnO ($\text{Zn}_{1-x}\text{Ni}_x\text{O}$) as nanowire arrays, but with low contents of nickel ($x \leq \sim 0.2$) and the retention of the wurtzite structure of ZnO. Equimolar ZnO–NiO mixtures in which both phases are preserved in the final nanocomposite have also been prepared by co-precipitation/co-gel formation techniques, and tested for the photocatalytic decolorization of dyes [11].

However, to date no low temperature synthesis method of a $\text{Ni}_{0.7}\text{Zn}_{0.3}\text{O}$ solid solution has been reported in the literature and this material has never been tested as a catalyst. To the best of our knowledge, this solid solution has only been tested for its photoluminescence [12] or electroluminescence [5] properties.

In this work we report for the first time the room-temperature synthesis of a high surface area $\text{Ni}_{0.7}\text{Zn}_{0.3}\text{O}$ solid solution by sacrificial template accelerated hydrolysis (STAH). The catalyst was synthesized on the surface of a stainless steel wire mesh of micrometer dimensions. Stainless steel wire mesh (SSWM)-supported metal oxide catalysts have been demonstrated in recent years by our group to be very promising structured catalytic systems [13–18]. We recently demonstrated the potential of the STAH technique to produce high surface area metal oxides using highly polar ZnO templates [19]. In that work we reported that weakly acidic cations (pK_a values below around -9.5 , such as Ni^{2+}) could only produce mixed oxides when deposited over a polar ZnO template, unlike the pure NiO obtained with non-polar ZnO nanowires [20,21]. As will be discussed below, it is the difference in local Zn^{2+} concentrations that appears to be the key to obtaining different products with both templates. The combination of a cheap and versatile support, such as SSWM, with a simple synthesis method, such as STAH, may lead to a process that is expected to be easily scalable and cost competitive for commercial applications.

To our knowledge the solid solution $\text{Ni}_{0.7}\text{Zn}_{0.3}\text{O}$ has never been tested in any catalytic process. In this study we analyzed it for the production of hydrogen via methanol steam reforming and methanol decomposition. These endothermic reactions are both possible routes for producing hydrogen on board fuel cell-based electric cars. Compared to methanol decomposition, methanol steam reforming requires a substantially higher amount of heat to vaporize the reactants, conduct the reaction, and compensate for heat loss from the reactor and the effluent streams. It is therefore more applicable in large-scale systems, where volumetric heat loss is lower than in small-scale devices [22]. For the decomposition of methanol, the heat for the reaction can be obtained by burning the carbon monoxide released, either in a preferential oxidation step or after it has been separated from the hydrogen stream in a catalytic membrane reactor [22]. Decomposed methanol can also be used as a source of synthesis gas for a number of chemical processes. The SSWM-supported metal oxide catalysts are ideal for use in micro-reactors for the generation of hydrogen by methanol decomposition, as has recently been reported with cobalt-based catalysts [14]. Nickel-based catalysts have also been successfully tested in this reaction [23–26]. In this work we show that a high surface area nickel–zinc solid solution may also be an interesting contender for onboard hydrogen production.

2. Experimental

2.1. Material preparation

All chemical reagents were of analytical grade and so were not subjected to additional purification. All of the aqueous solutions were prepared with deionized water. The support was a SSWM

[with a 30 μm wire diameter and a 40 μm screen opening] provided by CISA Cedaccia Industrial (www.cisa.net). The SSWM-supported polar ZnO with a yield of ~ 20 wt.% was synthesized as described in [18,19]. In this standard procedure, zinc acetate dihydrate was dissolved together with urea in deionized water. A Zn^{2+} concentration of 0.05 M was used in the aqueous solution, with a urea/ Zn^{2+} molar ratio of 20. The pH of the solution was adjusted to 4.88 by using acetic acid. The wire mesh was placed in a Teflon autoclave (100 mL) filled with the growth solution. The autoclave was sealed and hydrothermal ZnO growth was allowed to proceed at 80 °C for 23 h in a constant-temperature water bath. The ZnO coated-wire mesh was then taken out of the solution, thoroughly washed with deionized water and vacuum-dried at 60 °C. Finally the sample was calcined at 210 °C for 0.5 h in air.

In order to obtain samples with different ZnO yields, the standard method was modified by introducing changes in the synthesis temperature (60–90 °C) and in the Zn^{2+} concentration (0.025–0.2 M). Three templates were selected for the synthesis of SSWM-supported $\text{Ni}_{0.7}\text{Zn}_{0.3}\text{O}$ catalysts; SSWM-Z20, SSWM-Z35 and SSWM-Z40, acronyms used to designate SSWM-supported polar ZnO templates with approximately 20, 35 and 40 wt.% of ZnO, respectively. The ZnO yield was determined by weighing the samples.

To prepare the SSWM-supported nickel/zinc solid solution, the as-synthesized SSWM-supported ZnO templates with different ZnO yields were immersed in plastic flasks containing 50 mL water solutions of nickel nitrate. The closed flasks were subjected to shaking at RT in an orbital shaker for different periods of time. Subsequently, the samples were taken out of the flasks and washed with deionized water, vacuum-dried at 60 °C for 30 min and calcined in air at 300 °C for 2 h. The calcination temperature was selected on the basis of the TGA analysis of a synthesized Ni/Zn sample. Both the nickel-to-zinc molar ratio in the flasks ($R_{\text{Ni/Zn}}$ from 2 to 20) and the substitution time (t_s from 1 to 5 days) were varied in order to explore the effect of these variables on the final degree of nickel substitution. This optimization procedure was performed using the SSWM-Z20 template.

In some specific cases the ZnO phase remaining after the synthesis procedure was removed from the sample by washing it in a sodium hydroxide water solution (2 M) for 24 h.

2.2. Characterization

The chemical composition of the metal oxides was evaluated by means of atomic absorption spectroscopy (AAS, Shimadzu AA-6300). The morphology of the samples was studied by a scanning electron microscope (SEM, FEI Quanta FEG 650 model) and a transmission electron microscope (TEM, JEM-2100F) fitted with a detector for the EDS analysis. The X-ray diffraction (XRD) patterns of the catalysts were recorded on a Bruker D8 Advance instrument operating at 40 kV and 40 mA using Cu $K\alpha$ radiation ($\lambda = 0.15406$ nm). The crystal size values were estimated from the XRD pattern by means of Scherrer's equation (d_{XRD}). Instrumental contribution to line broadening was taken into account. The BET specific surface area of the samples was evaluated by means of N_2 adsorption isotherms (-196 °C) obtained on a Micromeritics ASAP 2020 analyser. The BET surface area was deduced from an analysis of the isotherms in the relative pressure range of 0.04–0.20.

Ex-situ X-ray photoelectron spectroscopy (XPS) was carried out on a Specs spectrometer, using Mg- $K\alpha$ or Al- $K\alpha$ (30 eV) radiation emitted from a double anode at 50 W. The binding energies of the resulting spectra were corrected using the binding energy of adventitious carbon (284.6 eV) in the C1s region. The backgrounds were subtracted by means of Shirley baselines. All the analyzed regions were deconvoluted by using mixed Gaussian–Lorentzian functions (90:10).

TPR analyses were performed in a chemisorption analyzer (Autochem II) equipped with a TCD detector. For each analysis the sample (8–10 mg of metal oxide) was first heated up to 400 °C in Argon, and then cooled down to 50 °C and treated with a 50 mL min⁻¹ stream of 10% H₂ in Argon from 50 °C to 600 °C at a rate of 5 °C min⁻¹.

2.3. Catalytic activity tests

Catalytic activity tests for methanol steam reforming (MSR) and methanol decomposition (MD) were performed in a six-flow parallel microrreactor system that allows up to six samples to be simultaneously tested by means of an automatic multiposition valve. Each catalyst consisted of a 5 × 1 cm² strip that was rolled up to form a 1 cm-high cylindrical piece. A roll of catalyst was then inserted into each of the six stainless-steel reactors (1/4 in. outer diameter). For both reactions the gas hourly space velocity was maintained in the range of 16,500–17,500 h⁻¹, the variations being due to small changes in the flow rates of the streams entering each reactor. Weight hourly space velocities ($g_{CH_3OH} g_{cat}^{-1} h^{-1}$), on a metal oxide mass basis, varied in the range 2.6–11.4 h⁻¹, depending on the reaction tested and on the amount of catalyst loaded onto the metal wire mesh.

Each reactor was fed with a stream of 7 vol.% CH₃OH + 8 vol.% H₂O (MSR) or 10 vol.% CH₃OH (MD) plus 10 vol.% Ar and He to balance. The samples were first heated in a flow of He at 300 °C during the calibration step, which lasted around 5 h. Then the catalysts were subjected to the following isothermal steps: 300–350–400–450–400–350–300 °C (MSR, 15-h steps) or 225–250–275–300–325–300–275–250–225 °C (MD, 10-h steps). The transition ramp between each temperature step was performed under a helium atmosphere. The products were analyzed online by mass spectrometry (Omnistar 3000). CH₃OH, H₂, CO, CO₂, CH₄, H₂O and O₂ were quantitatively analyzed with the help of previous calibration steps, whereas the evolution of formaldehyde, dimethyl-ether (DME) and methyl-formate (MF) was tracked from the changes in the mass intensities of fragments 60 (MF), 46 (DME) and the ratio of the intensities of the fragments 30 to 31 (formaldehyde). This procedure allowed an accurate assessment of the carbon-products formed during the reaction different from CO, CO₂ and CH₄.

The methanol conversion parameter (X_{MeOH} ; %) represents the percentage of methanol converted during the process taking into account the difference between the total flow rates at the outlet and the inlet of the reactor (F^{out} and F^{in} , respectively, in mL min⁻¹):

$$X_{MeOH} = 100 \times \left(1 - \frac{F^{out}}{F^{in}} \frac{C_{MeOH}^{out}}{C_{MeOH}^{in}} \right) \quad (1)$$

where C_{MeOH}^{in} and C_{MeOH}^{out} are the concentrations of methanol (vol.%) in the inlet and in the outlet gas stream, respectively. F^{out}/F^{in} can be evaluated as follows:

$$\frac{F^{out}}{F^{in}} = \frac{A_1 B_2 - A_2 B_1}{A_3 B_2 - A_2 B_3} \quad (2)$$

or, alternatively, for the case discussed below, as follows:

$$\frac{F^{out}}{F^{in}} = \frac{A_1}{A_3} = \frac{B_1}{B_3} \quad (3)$$

where parameters A_i and B_i are evaluated from the following expressions:

$$A_1 = C_{MeOH}^{in} \quad (4)$$

$$A_2 = -\nu \quad (5)$$

$$A_3 = C_{MeOH}^{out} + C_{CO}^{out} + C_{CO_2}^{out} + C_{CH_4}^{out} \quad (6)$$

$$B_1 = C_{MeOH}^{in} + C_{H_2O}^{in} \quad (7)$$

$$B_2 = -\rho \quad (8)$$

$$B_3 = C_{MeOH}^{out} + C_{H_2O}^{out} + 2 C_{CO_2}^{out} + C_{CO}^{out} \quad (9)$$

In these equations, C_i^{out} (i : CO, CO₂, CH₄, H₂O) corresponds to the outlet concentration of i species, while C_i^{in} corresponds to its concentration (vol.%) in the inlet gas stream. Parameters ν and ρ are the number of carbon and oxygen atoms, respectively, of a carbon-containing molecule $C_\nu H_\mu O_\rho$ that may be formed during the process, apart from CO, CO₂ or CH₄, assuming that only one type of molecule will be formed. Thus, if this molecule is formed, F^{out}/F^{in} must be calculated by means of Eq. (2), whereas, in the absence of this molecule, any of the equations in (3) may be used. The concentration of this molecule (the presence of which can be detected by the mass spectrometer but not quantitatively evaluated) can be determined by means of the following equation:

$$C_{C_\nu H_\mu O_\rho}^{out} = \frac{A_1 B_3 - A_3 B_1}{A_1 B_2 - A_2 B_1} \quad (10)$$

In this way, both the variation in the flow rate as a consequence of the reaction (the importance of which was underlined in a previous work [27]) and the formation of a species not quantified but detected by the analytical system can be considered when calculating of the methanol conversion via Eq. (1).

The hydrogen yield, which depends on the type of reaction being analysed, can be evaluated from:

$$X_{H_2} = 100 \times \frac{F_{H_2}^{out}}{\alpha F_{MeOH}^{in}} \quad (11)$$

where $F_{H_2}^{out}$ is the hydrogen flow rate at the outlet of the reactor and parameter α takes the value of 3 in the MSR reaction ($CH_3OH + H_2O \rightarrow CO_2 + 3 H_2$) and 2 in the MD reaction ($CH_3OH \rightarrow CO + 2 H_2$).

Finally, carbon selectivity towards the different carbon-containing species can be evaluated as follows:

$$S_{CO}^C = 100 \times \frac{C_{CO}^{out}}{C_{CO}^{out} + C_{CO_2}^{out} + C_{CH_4}^{out} + \nu C_{C_\nu H_\mu O_\rho}^{out}} \quad (12)$$

$$S_{CO_2}^C = 100 \times \frac{C_{CO_2}^{out}}{C_{CO}^{out} + C_{CO_2}^{out} + C_{CH_4}^{out} + \nu C_{C_\nu H_\mu O_\rho}^{out}} \quad (13)$$

$$S_{CH_4}^C = 100 \times \frac{C_{CH_4}^{out}}{C_{CO}^{out} + C_{CO_2}^{out} + C_{CH_4}^{out} + \nu C_{C_\nu H_\mu O_\rho}^{out}} \quad (14)$$

$$S_{C_\nu H_\mu O_\rho}^C = 100 \times \frac{\nu C_{C_\nu H_\mu O_\rho}^{out}}{C_{CO}^{out} + C_{CO_2}^{out} + C_{CH_4}^{out} + \nu C_{C_\nu H_\mu O_\rho}^{out}} \quad (15)$$

The thermal conversion of methanol in the analyzed temperature range was not detected in any of the experiments performed without a catalyst. To compare the catalytic activities obtained in this work with those reported elsewhere, we employed a simple first order reaction rate equation, which for an integral reactor yields the following expression for the catalytic rate constant of methanol decomposition:

$$(16) k_{md} = - \frac{\nu_{in}}{w_{cat} \times P_{MeOH}^{in}} \times \ln \left(1 - \frac{X_{MeOH}}{100} \right) \text{ where } \nu_{in} \text{ is the inlet molar flow rate of methanol (mol s}^{-1}\text{), } w_{cat} \text{ is the catalyst weight (g) (excluding the SSWM support) and } P_{MeOH}^{in} \text{ is the inlet partial pressure of methanol (Pa).}$$

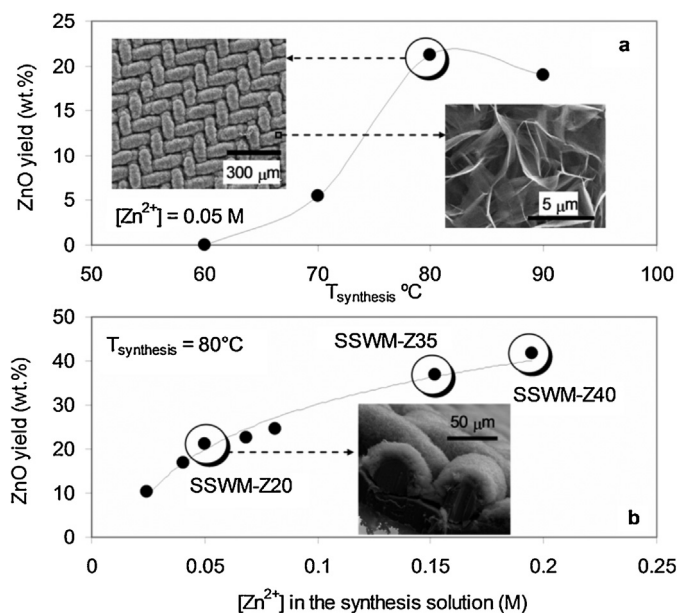


Fig. 1. Variation of the ZnO yield (a) with the synthesis temperature (a) and the concentration of Zn^{2+} in the synthesis solution used for the fabrication of the SSWM-supported ZnO template. Insets: SEM images of the sample prepared at 80°C and $[\text{Zn}^{2+}] = 0.05 \text{ M}$.

3. Discussion of results

3.1. Optimization of the ZnO yield in the templates

The SSWM–ZnO template prepared according to the standard procedure described in Section 2 is composed of arrays of ZnO nanosheets forming a layer with a thickness of $\sim 13 \mu\text{m}$ that covers the SSWM surface (SEM images in Fig. 1), show good adhesion to the support and have a large proportion of polar surfaces [19]. The ZnO on the SSWM has a yield of $\sim 20 \text{ wt.}\%$, a BET specific surface area of between 60 and $80 \text{ m}^2 \text{ g}^{-1}$ (on a ZnO mass basis) and a crystal size of $d_{\text{XRD}} = \sim 13 \text{ nm}$. A preliminary step for maximizing the ZnO yield in the SSWM–ZnO supported template was performed by varying the synthesis temperature and the precursor (zinc acetate) concentration. Fig. 1a shows the optimum synthesis temperature to be 80°C , as in the original procedure described in Section 2. At this temperature, an increase in the precursor concentration produced a concomitant increase in the ZnO yield, up to values of over 40 wt.% within the concentration range analysed (Fig. 1b). The specific surface area of ZnO in the materials obtained was maintained regardless of the value of the ZnO yield. The templates outlined in Fig. 1b were selected for preparing catalysts with different loads of $\text{Ni}_{0.7}\text{Zn}_{0.3}\text{O}$ on the SSWM support, that would allow the WHSV

values to be changed during the catalytic tests while the gas hourly space velocity was kept constant.

3.2. Synthesis and characterization of the SSWM-supported $\text{Ni}_{0.7}\text{Zn}_{0.3}\text{O}$

Since all the preparations were performed at room temperature and ambient pressure, the main substitution parameters used when applying the STA method with the polar SSWM–Z20 template were (i) the aqueous nickel ion to zinc molar ratio ($R_{\text{Ni/Zn}}$) and (ii) the substitution time (t_s). Using nickel acetate solutions our objective was to prepare the pure metal oxide, as we did with iron, titanium, cerium and copper oxides in [19]. Fig. 2a shows the substitution degrees ($\text{Ni}/(\text{Ni} + \text{Zn})$ molar ratio in the obtained samples) for a value of $R_{\text{Ni/Zn}} = 7$ and different substitution times (1 to 10 days). It can be seen from this figure that the maximum exchangeable ratio is approximately 0.6. It was expected that higher values of $R_{\text{Ni/Zn}}$ in the synthesis solution would increase this ratio but, as can be seen in Fig. 2b, the limit of 0.6 is still maintained. Even an increase of the synthesis temperature to 90°C failed to yield the expected increase in the substitution degree. To check whether the remaining zinc was in the form of zincite or not, the sample represented by the circle enclosed in the dashed box of Fig. 2b was washed with a solution of NaOH (2 M). As a result the $\text{Ni}/(\text{Zn} + \text{Ni})$ molar ratio increased but only from 0.61 to 0.68 (triangle enclosed in the dashed box of Fig. 2b) indicating that the zinc present in the original sample was hardly in the form of soluble zincite. The XRD patterns of the sample, before and after washing, are displayed in Fig. 3, the upper plot corresponding to the unwashed sample (a macroscopic image of which is shown in the inset). The spectrum is made up of three phases: a small fraction of zincite (PDF no. 01-075-0576), a major fraction of $\text{Ni}_{0.7}\text{Zn}_{0.3}\text{O}$ (PDF no. 01-075-0272) and the support (SSWM). As expected, in the washed sample the spectrum of zincite is absent. In view of this result and the $\text{Ni}/(\text{Zn} + \text{Ni})$ molar ratios of both samples (0.61 and 0.68), it can be concluded that the original sample was composed of around 90 mol% $\text{Ni}_{0.7}\text{Zn}_{0.3}\text{O}$ and 10 mol% ZnO. The yield of metal oxides in the washed sample decreased from $\sim 21 \text{ wt.}\%$ (original sample) to $\sim 15 \text{ wt.}\%$, which means that the disappearance of ZnO was accompanied by the loss of some $\text{Ni}_{0.7}\text{Zn}_{0.3}\text{O}$. This suggests that at least a part of the unreacted ZnO in the original sample became bonded to the SSWM, serving as a link between the mesh and part of the $\text{Ni}_{0.7}\text{Zn}_{0.3}\text{O}$ phase.

Fig. 4 shows the TPR profile of the washed sample. Three main peaks were obtained by applying a deconvolution procedure, with maxima at 167, 285 and 347°C . The low temperature peak can be attributed to non-stoichiometric oxygen on the surface (Ni^{3+} ions) [28,29], the peak at 285°C to easily reducible surface Ni^{2+} (that which was originally present and that which originated from the reduction of Ni^{3+}) and the high temperature

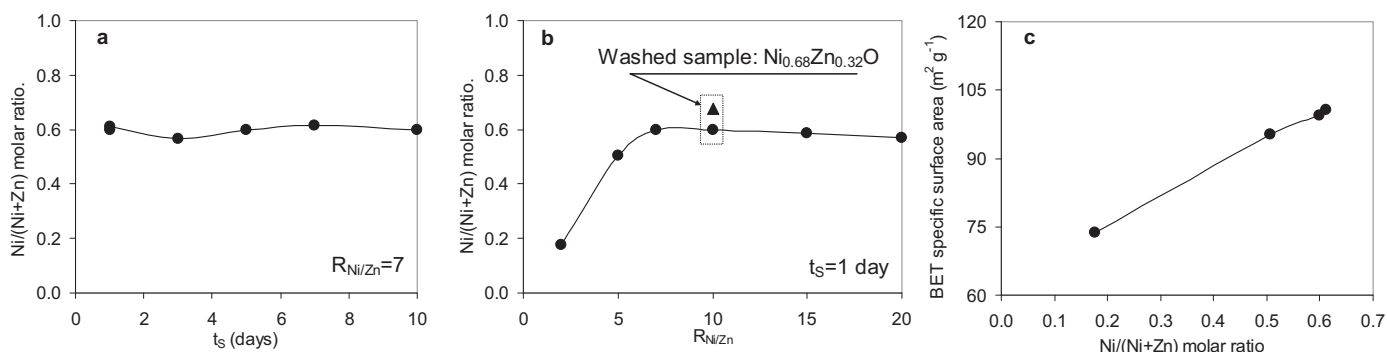


Fig. 2. Effect of (a) substitution time (t_s) and (b) $R_{\text{Ni/Zn}}$ on the degree of nickel substitution. (c) Variation of the specific surface area with the degree of nickel substitution.

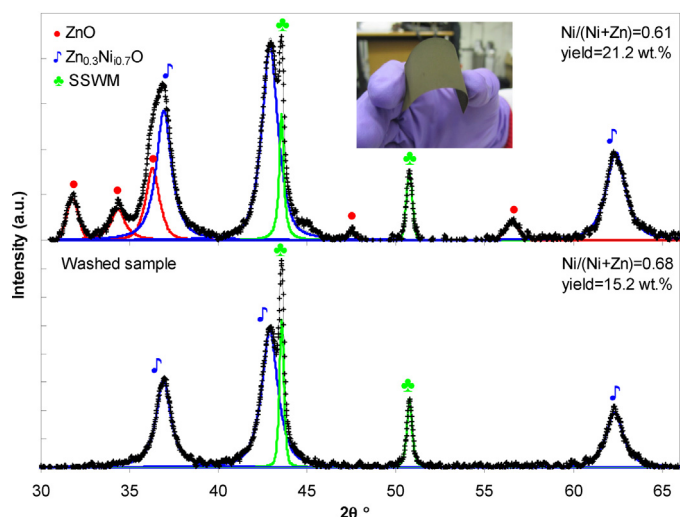


Fig. 3. XRD spectra of (a) an as-prepared SSWM-supported $\text{Ni}_{0.7}\text{Zn}_{0.3}\text{O}$ sample and (b) the same sample after being washed with NaOH (2 M). Inset in (a) photograph of the original sample showing its flexibility.

peak is ascribed to bulk Ni^{2+} [30]. Zn^{2+} is not reducible in this temperature range, as confirmed by the TPR analysis of the SSWM-Z20 template. The peak distribution shown in Fig. 4 corresponds to the reduction of a species with the chemical formula $\text{Zn}^{2+}_{0.3}\text{Ni}^{2+}_{\text{[bulk]}}_{0.283}\text{Ni}^{2+}_{\text{[surf]}}_{0.249}\text{Ni}^{3+}_{0.168}\text{O}_{1.084}$ with a relative error of $\sim 3\%$ for the total hydrogen consumption. This means that around 60% of the nickel atoms are located on the external surface of the sample, which is consistent with the low crystal size value obtained by applying Scherrer's equation to the spectra shown in Fig. 3 ($d_{\text{XRD}} = 8 \text{ nm}$) and with the high values of specific surface area in Fig. 2c. As occurred with most of the metal oxides synthesized in a previous work [19], the specific surface area increases with the degree of nickel substitution up to values of around $100 \text{ m}^2 \text{ g}^{-1}$ for the fully developed solid solution.

XPS was also used to gain a better insight into the structure of the solid solution. Fig. 5 shows the $\text{Ni}2p_{3/2}$ spectra obtained for the washed sample by using Mg- $K\alpha$ and Al- $K\alpha$ radiation sources. The deconvolution parameters obtained for this and the rest of the XPS regions analyzed are indicated in Table 1. As can be seen, the main peaks are located at around 852.9–853.3 eV (no. 1), 854.3–854.7 eV (no. 2) and 856.2–856.5 eV (no. 3). Peak no. 2 at $\sim 854.5 \text{ eV}$, which is close to what one would expect for NiO [29–31], is ascribed to octahedral Ni^{2+} forming part of the external surface of the particles. This is corroborated by the different area ratio values for the main peaks (no. 1/2) obtained with both X-ray sources (Fig. 5). The lower relative area of peak no. 2 was obtained from the Al source, indicating that the species that gave rise to this peak was more

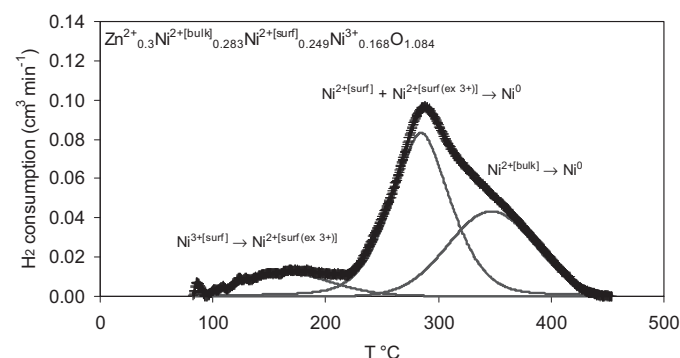


Fig. 4. TPR profile of a NaOH-washed SSWM-supported $\text{Ni}_{0.7}\text{Zn}_{0.3}\text{O}$ sample.

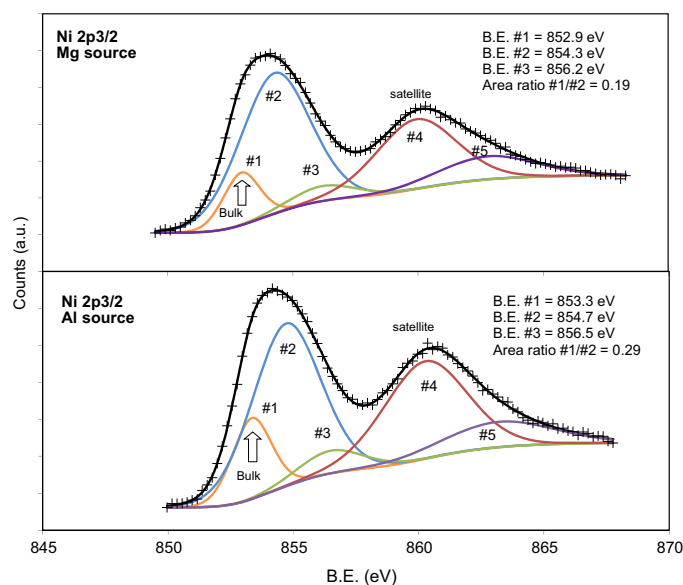


Fig. 5. XPS spectra with two different radiation sources in the $\text{Ni}2p_{3/2}$ region of a NaOH-washed SSWM-supported $\text{Ni}_{0.7}\text{Zn}_{0.3}\text{O}$ sample.

concentrated on the external surface of the particles. Peak no. 3 at $\sim 856.4 \text{ eV}$ is attributed to the Ni^{3+} species [29,32], which were also detected by TPR (Fig. 4), while peaks no. 4 and 5 are satellite peaks.

The $\text{O}1s$ spectra (Fig. 6) corroborate the results reported above; peak no. 2 located at 530.6 eV is ascribed to oxygen linked to octahedral Ni^{2+} [32,33], which is more concentrated at the surface of the particles than inside the bulk (the no. 2/1 peak area ratio decreases when using the Al radiation source), whereas peak no. 3 at $\sim 536.7 \text{ eV}$ is attributed to non-stoichiometric oxygen linked to Ni^{3+} cations [32,33].

Finally, the $\text{Zn}2p$ spectrum (Fig. 7) shows two main peaks at 1020.2 and 1043.3 eV (peaks no. 1 and 4) and two small peaks located at 1022.5 and 1044.5 eV (peaks no. 2 and 5 in Fig. 7). Octahedral Zn^{2+} in $\text{Ni}_{0.7}\text{Zn}_{0.3}\text{O}$ obtained at high temperature has a binding energy in the $\text{Zn}2p_{3/2}$ region of 1021.6 eV [3], for an assumed binding energy of the associated oxygen in the $\text{O}1s$ region of 529.5 eV

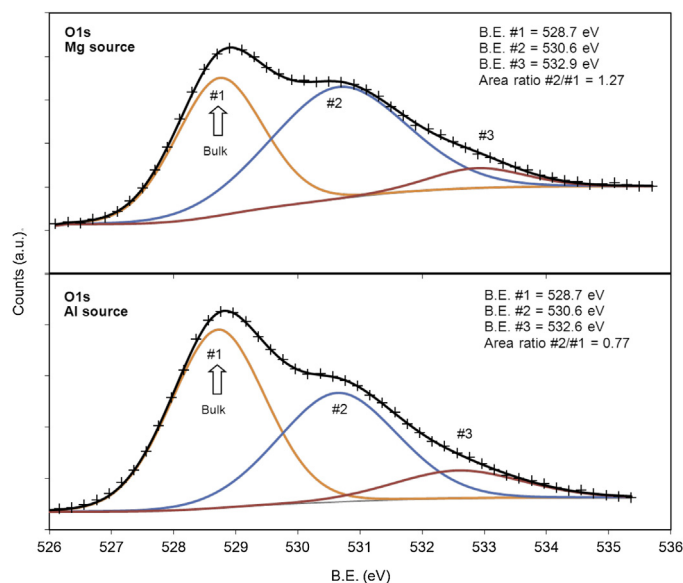


Fig. 6. XPS spectra with two different radiation sources in the $\text{O}1s$ region of a NaOH-washed SSWM-supported $\text{Ni}_{0.7}\text{Zn}_{0.3}\text{O}$ sample.

Table 1
Deconvolution parameters for the XPS analysis of a NaOH-washed SSWM-supported $\text{Ni}_{0.7}\text{Zn}_{0.3}\text{O}$ sample.

XPS region	Peak no.	Mg-K α source		Al-K α source	
		B.E. (eV)	Total area fraction	B.E. (eV)	Total area fraction
$\text{Ni}2\text{p}_{3/2}$	1	852.9	0.09	853.3	0.12
	2	854.3	0.49	854.7	0.42
	3	856.2	0.05	856.5	0.06
	4	859.9	0.27	860.3	0.31
	5	862.8	0.11	863.2	0.11
O1s	1	528.7	0.41	528.7	0.51
	2	530.6	0.52	530.6	0.39
	3	532.9	0.07	532.6	0.11
$\text{Zn}2\text{p}_{3/2}$	1	1020.2	0.52	–	–
	2	1022.5	0.05	–	–
	3	1035.1	0.09	–	–
$\text{Zn}2\text{p}_{1/2}$	4	1043.3	0.28	–	–
	5	1045.5	0.06	–	–

[3]. On the other hand, tetrahedral ZnO has binding energies of 1022.6 eV ($\text{Zn}2\text{p}_{3/2}$), 1045.6 eV ($\text{Zn}2\text{p}_{1/2}$) and 530.0 eV (O1s) [34]. It seems clear that the small peaks no. 2 and 5 (Fig. 7) must be attributed to residual zincite (tetrahedral ZnO), but the low binding energy peaks cannot be ascribed to fully coordinated octahedral Zn^{2+} .

A feature common to the spectra in Figs. 5–7, and rarely mentioned in the literature, is the presence of low binding energy peaks with no obvious assignation, i.e., those indicated by arrows in the figures. Peak no. 1 in the $\text{Ni}2\text{p}_{3/2}$ spectra (852.9–853.3 eV) cannot be ascribed to metallic Ni, which has a lower binding energy [31,35]. De Jesús et al. [36] detected this peak in nickel oxide films oxidized at room temperature while they were being subjected to argon ion bombardment. The O1s peak for the same sample was 529.1 eV [36], which is also very similar to peak no. 1 in the O1s spectra in Fig. 6. These authors attributed the low binding energy peaks to the partial reduction of the nickel oxide as a consequence of argon ion bombardment. A similar observation was made by Li et al. [37] with respect to thin air annealed-ZnO

films. When the samples experienced some reduction (loss of oxygen) they detected a clear decrease in binding energy in both the peak in the O1s region (from 530.8 to 529.9 eV) and the peak in the $\text{Zn}2\text{p}_{3/2}$ region (from 1022.4 to 1021.5 eV) with respect to the unreduced sample. Remashan et al. [38], working with N_2O plasma-treated ZnO thin films observed low binding energy peaks in the O1s (529.5 eV) and $\text{Zn}2\text{p}_{3/2}$ (1020.2 eV) regions, similar to peaks no. 1 in Figs. 6 and 7, which, on the basis of previously published reports, they also attributed to a greater number of zinc atoms being bound to oxygen. These data support the hypothesis of a bulk rock-salt crystal structure with oxygen vacancies, in which most of the octahedral Zn^{2+} cations (peak no. 1 in Fig. 7 holds most of the area of the $\text{Zn}2\text{p}_{3/2}$ region) and part of the Ni^{2+} cations are in a slightly reduced state. An ideal representation of this structure is shown as an inset in Fig. 7.

In the light of these new results, the empirical formula of the solid solution derived from the TPR results must now be changed slightly to:

$$\text{Zn}^{(2-\sigma)+}_{0.30}\text{Ni}^{(2-\delta)+[\text{bulk}]}_{0.28}\text{Ni}^{2+[\text{surf}]}_{0.25}\text{Ni}^{3+}_{0.17}\text{O}_{1.085-0.15\sigma-0.14\delta}$$

in which approximately the same number of zinc and nickel cations are affected by the oxygen vacancies in the rocksalt crystal structure.

The morphology, particle size and chemical make-up of the as-prepared solid solution were studied by SEM and EDS-assisted TEM analysis, the results of which are shown in Fig. 8. A comparison of Figs. 1a and 8a reveals that the macroscopic morphology of the ZnO template is approximately unchanged after the synthesis. The mixed oxide is arranged in arrays of thin sheets of homogenous length in the 5–7 μm range.

TEM images of the solid solution are shown in Fig. 8b and c. The sample is formed by three-dimensionally interconnected nanograins of size ~ 7 nm which give rise to a high porosity in the macroscopic nanosheets. This result is in good agreement with the crystal size evaluated by XRD ($d_{\text{XRD}} = 8$ nm). The lattice spacing observed in Fig. 8c is approximately 2.1 Å, which corresponds to the (200) plane of the rocksalt crystal structure in NiO.

The composition of the mixed oxide was analysed using a dispersive X-ray spectroscopy (EDS) line scan profile of Ni, Zn and O (Fig. 8b). The parallel location of nickel and zinc throughout the nanoparticle demonstrates that there is a homogenous distribution of Ni and Zn with a $\text{Ni}/(\text{Zn} + \text{Ni})$ atom ratio that is in fair agreement with that of the AAS analysis.

The exact mechanism by which the solid solution is formed by room-temperature sacrificial template accelerated hydrolysis is unclear. The hydrolysis of nickel ions provides nickel hydroxide complexes and H^+ in the surroundings of the ZnO template, which is simultaneously etched by the protons to form Zn^{2+} . This

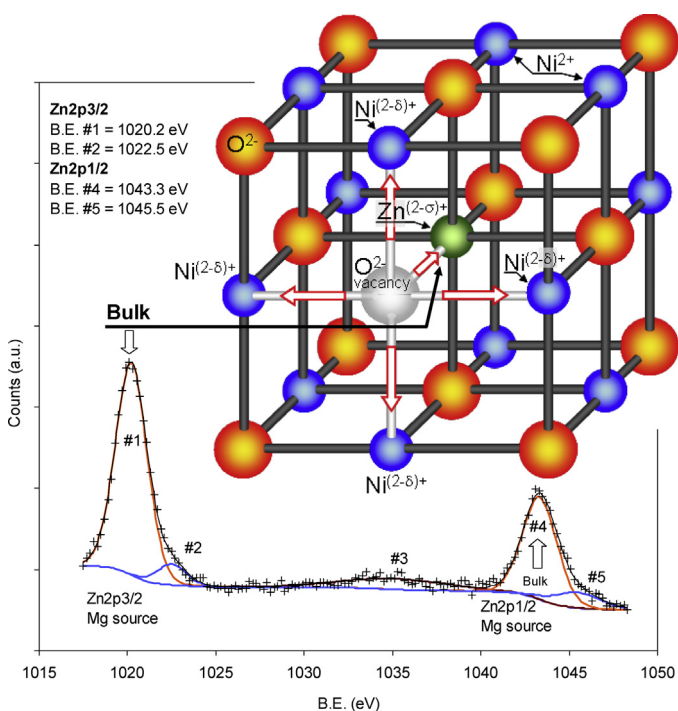


Fig. 7. XPS spectra in the Zn2p region of a NaOH-washed SSWM-supported $\text{Ni}_{0.7}\text{Zn}_{0.3}\text{O}$ sample. Inset: crystal structure of the bulk $\text{Ni}_{0.7}\text{Zn}_{0.3}\text{O}$.

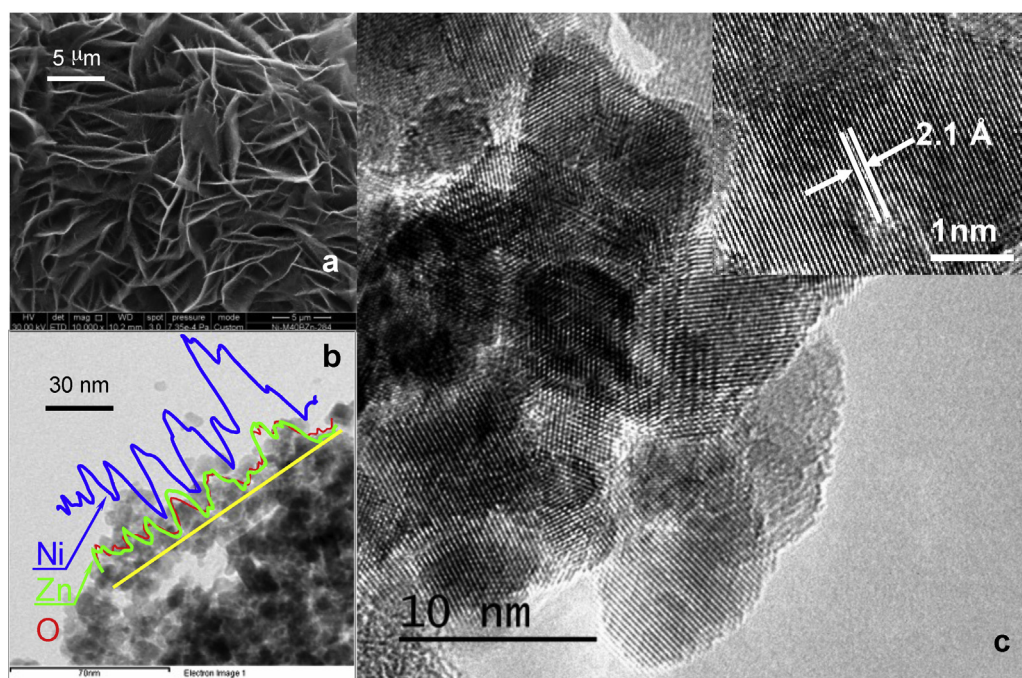


Fig. 8. (a) SEM image of the as-prepared SSWM-supported $\text{Ni}_{0.7}\text{Zn}_{0.3}\text{O}$ sample. (b) EDS analysis of the same sample performed in a TEM microscope. (c) TEM images of the same sample.

consumption of H^+ accelerates the hydrolysis process of the Ni^{2+} , leading to an enhancement of the etching process of ZnO . As a result, nickel hydroxide complexes precipitate onto the ZnO scaffold, to form the early rigid framework of the nanosheets. We suggest that a combination of a low hydrolysis rate (nickel is a weakly acidic cation) and the high local concentration of Zn^{2+} originating from the dissolution of the highly polar ZnO template allows the nickel hydroxides being formed to trap the Zn^{2+} ions within their crystal structure. This phenomenon does not take place when non-polar ZnO nanowires are used [20,21], probably due to a much lower local Zn^{2+} concentration. Progressive hydrolysis and the dissolution of the template eventually result in the high surface area $\text{Ni}_{0.7}\text{Zn}_{0.3}\text{O}$ nanosheet-based architectures displayed in Fig. 8a.

3.3. Catalytic production of hydrogen from methanol

For the catalytic tests three different catalysts were used: SSWM-Ni20, SSWM-Ni35 and SSWM-Ni40. These samples were prepared by applying sacrificial template synthesis at RT from SSWM-Z20, SSWM-Z35 and SSWM-Z40, respectively, for $t_s = 1$ day and $R_{\text{Ni/Zn}} = 7$, with $\text{Ni}_{0.7}\text{Zn}_{0.3}\text{O}$ yields of 20.2, 35.2 and 41 wt.%, respectively. In all the experiments the same gas hourly space velocity (GHSV) was kept constant. Because three catalysts with different active phase yields were used, it was possible to study the effect of the changes in weight hourly space velocity (WHSV) on the reactions. The pure SSWM-supported ZnO catalyst was found to be almost inactive in the tested processes. As an example, the reaction rate constant for methanol decomposition of SSWM-supported ZnO was found to be two orders of magnitude lower than that of the $\text{Ni}_{0.7}\text{Zn}_{0.3}\text{O}$ -based catalysts.

Fig. 9 offers the variation of reaction temperature, methanol conversion (Eq. (1)) and hydrogen yield (Eq. (11)) with time for the SSWM-Ni35 catalyst tested in the methanol steam reforming reaction (MSR) and in the methanol decomposition reaction (MD). The same experimental sequence was used for testing the rest of catalysts. The conversion points displayed in the ensuing figures are those corresponding to the end of each isothermal stage

(i.e., diamonds in the MSR curves of Fig. 9). The catalyst shows a good stability in the steam reforming reaction and a certain degree of deactivation in the methanol decomposition reaction, the cause of which will be discussed below.

Fig. 10 shows the results of methanol conversion and hydrogen yield in the MSR reaction for the SSWM-supported $\text{Ni}_{0.7}\text{Zn}_{0.3}\text{O}$ catalysts with different yields (SSWM-Z20, SSWM-Z35 and SSWM-Z40) after 15 h of reaction at the given temperatures (i.e., diamonds in Fig. 9). The arrows indicate the direction of the experimental

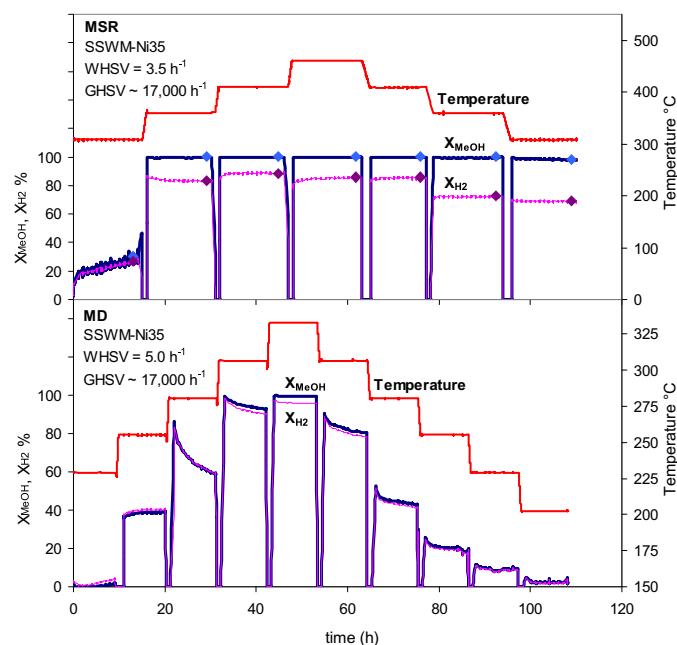


Fig. 9. Variation of reaction temperature, methanol conversion and hydrogen yield with time for the SSWM-Ni35 catalyst tested in the methanol steam reforming reaction (MSR) and in the methanol decomposition reaction (MD).

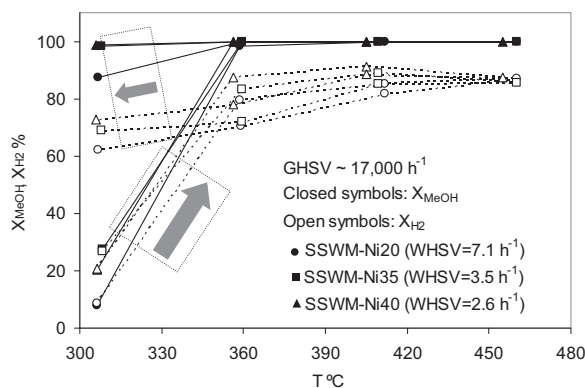


Fig. 10. Variation of methanol conversion and hydrogen yield with temperature for the catalysts tested in the methanol steam reforming reaction. The arrows indicate the direction of the experimental sequence.

sequence. It can be seen that, when the temperature is increased, there is a marked increment in methanol conversion between 300 and 350 °C, as a consequence of the reduction of nickel oxide. At temperatures over 350 °C there is a complete conversion of methanol which is maintained when the temperature is reduced again to ~300 °C for the lowest WHSV values (SSWM-Ni35 and SSWM-Ni40). The hydrogen yield, which, as expected, is dependent to some extent on the WHSV, shows values somewhat below those of the methanol conversion, although it reaches values close to 90% at temperatures of around 400 °C. The cause for this discrepancy between hydrogen yield and methanol conversion is the carbon selectivity. As can be seen in Fig. 11, the carbon selectivity towards CO (methanol decomposition reaction: $\text{CH}_3\text{OH} \rightarrow \text{CO} + 2\text{H}_2$) is high at temperatures below 400 °C, but it decreases in favour of the carbon selectivity towards CO_2 at increasing reaction temperatures and decreasing WHSV values. Thus the methanol decomposition reaction is favoured over the water gas shift reaction ($\text{CO} + \text{H}_2\text{O} \leftrightarrow \text{CO}_2 + \text{H}_2$) at high values of weight hourly space velocity and low temperatures. This suggests that the steam reforming process needs longer contact times and/or higher steam pressures for the water gas shift reaction to proceed to the right, which causes the H_2 yield and the carbon selectivity towards CO_2 to increase. The longer contact time can be tested by increasing the gas hourly space velocity. This can be easily done in view of the modularity of the monolithic SSWM-supported catalysts. At temperatures over 400 °C the carbon selectivity towards CO seems to have a bottom limit of around 42% at the GHSV tested in this work, probably due to thermodynamic constraints. Therefore, the temperature zone between 350 and 400 °C seems in principle to be the most appropriate range for investigating the effect of the GHSV and/or the steam pressure on the carbon selectivity towards CO_2 , considering that at higher temperatures carbon selectivity towards methane, though low, starts to become noticeable, especially at the lowest WGSV, something which was recognized long ago in methanol decomposition reactions over nickel-based catalysts [39]. However, this issue will be addressed in more detail in a future work on a micro-reactor specifically designed for this type of monolithic catalysts. The analytical system also detected some traces of dimethyl-ether that decreased with a rise in temperature. Application of Eq. (10) yielded concentration values for this compound very close to zero.

It is evident from the results discussed above that the tested catalysts are active in the methanol decomposition reaction over the temperature range analyzed. This reaction was studied in separate experiments, as pointed out in Section 2, the results of which are shown in Figs. 12 and 13. Fig. 12a shows the variation in methanol conversion and hydrogen yield for the different catalysts after 10 h of reaction at the given temperatures. Both curves are similar,

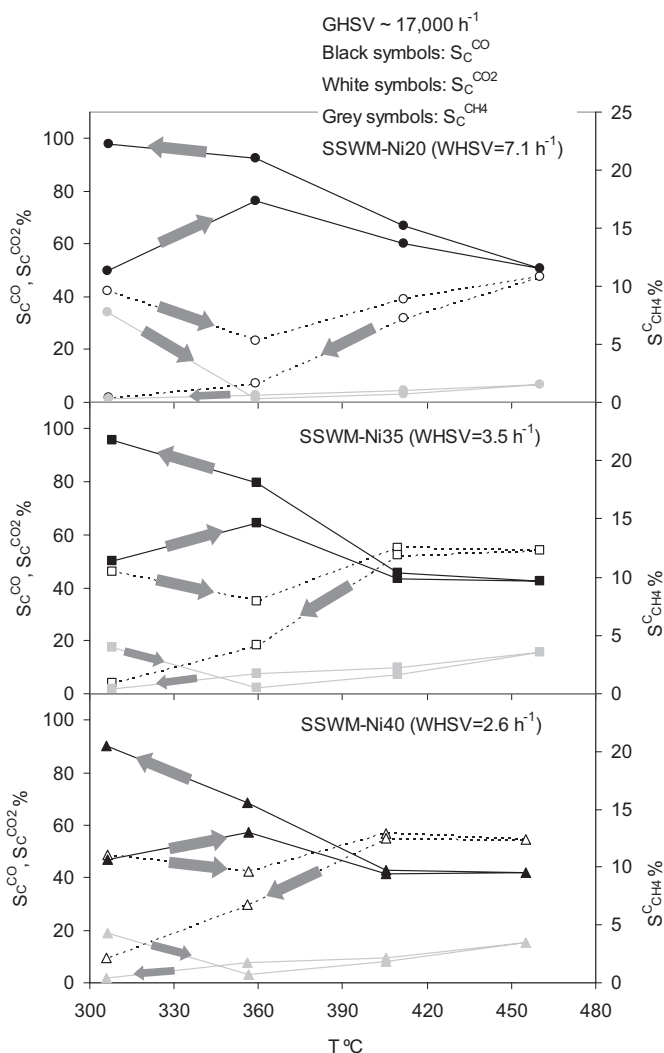


Fig. 11. Variation of carbon selectivity towards CO, CO_2 and CH_4 with temperature for the catalysts tested in the methanol steam reforming reaction. The arrows indicate the direction of the experimental sequence.

which is a clear indication of the high carbon selectivity towards carbon monoxide, over 97% for all catalysts in the range of temperatures analyzed. At the highest temperatures a small amount of methane was detected ($S_{\text{CH}_4}^{\text{C}} < 2\%$), as a result of the methanation reaction ($\text{CO} + 3\text{H}_2 \leftrightarrow \text{CH}_4 + \text{H}_2\text{O}$) [40]. At some low temperatures the hydrogen yield was slightly higher than the methanol conversion, due to the experimental error of the analytical method. As expected, the methanol conversion increases at lower values of WHSV. In all the experiments, the values of methanol conversion collected at increasing temperatures are higher than those obtained in the subsequent sequence at decreasing temperatures, as exemplified by the data for SSWM-Ni40 in Fig. 12a. A similar trend was observed for the hydrogen yield in the methanol steam reforming reaction (Fig. 10), once the onset of nickel reduction was surpassed ($T > 330$ °C); in this case it is probably due to a higher reduction degree of the catalyst surface leading to an increase in the carbon selectivity to CO in the sequence at decreasing temperatures (Fig. 11) and not to catalyst deactivation. As can be seen in Fig. 12a, the onset of nickel oxide reduction occurs at a rather lower temperature in the absence of steam (~250 °C). The lower conversion degrees in the sequence of decreasing temperatures are due in this case to gradual deactivation of the catalysts during the experimental sequence (MD curves in Fig. 9) as a consequence of coke deposits.

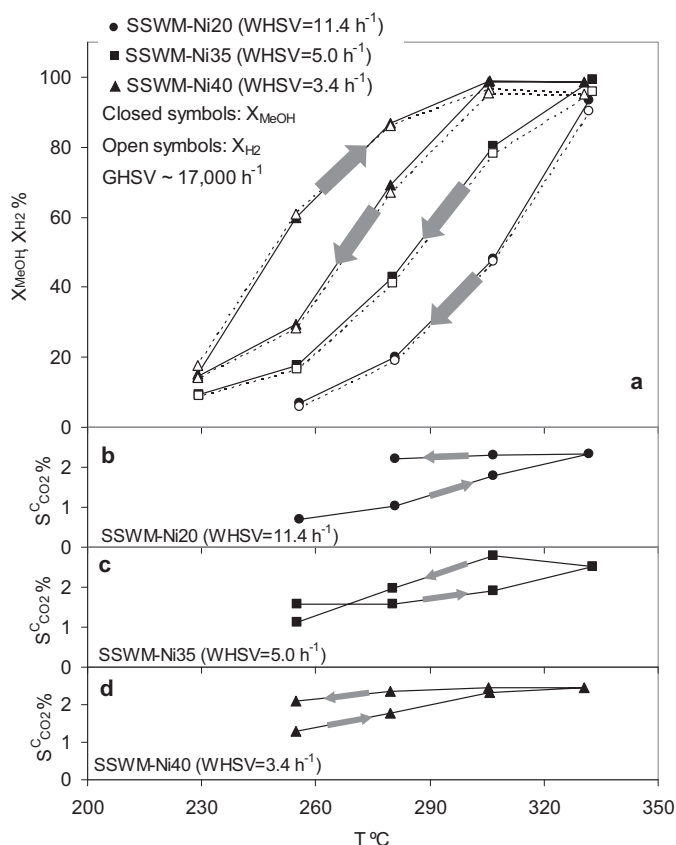


Fig. 12. Variation of (a) methanol conversion and hydrogen yield and (b)–(d) carbon selectivity towards CO_2 with temperature for the catalysts tested in the methanol decomposition reaction. The arrows indicate the direction of the experimental sequence.

This is inferred from the low, though conspicuous, values of carbon selectivity towards CO_2 , plotted in Fig. 12b to d for values of methanol conversion of over 15%. CO_2 is formed on reduced nickel centres via the Boudouard equilibrium ($2\text{CO} \leftrightarrow \text{C} + \text{CO}_2$) [40]. As can be observed in the figures, the amount of CO_2 released increases with the temperature and as the reaction proceeds, the latter being a consequence of the greater availability of reduced nickel centres.

To calculate the methanol decomposition constant, the more conservative values of the sequence at decreasing temperatures

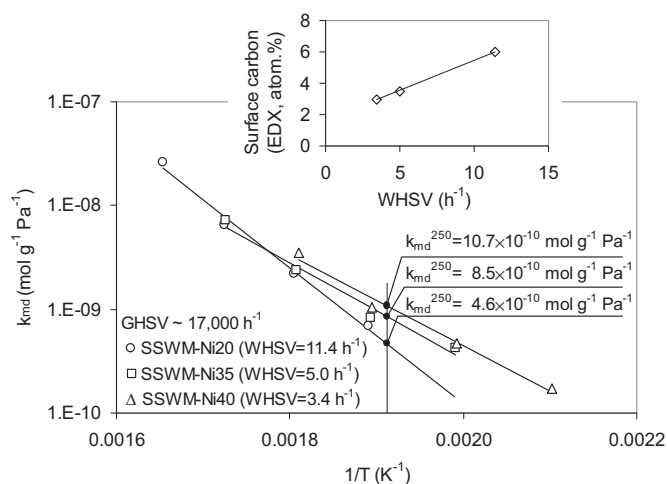


Fig. 13. Arrhenius plot of the methanol decomposition constant (Eq. (16)) for the catalysts tested. Inset: variation of the surface carbon content with the weight hourly space velocity after a complete experimental sequence of methanol decomposition.

were used. Fig. 13 shows an Arrhenius plot with the k_{md} values obtained for the different catalysts (Eq. (16)). This is an intrinsic constant that should be independent of the active phase yield or WGHV. However, Fig. 13 shows that there is a slight dependence of catalytic performance on these variables. The reason for this dependence is the different degrees of catalyst deactivation due to coke deposition for different values of WGHV. EDX analyses of the surface of the catalysts after a complete reaction sequence show an increase in carbon content for increasing values of WHSV (inset in Fig. 13), which explains the higher deactivation degree of SSWM-Ni20 compared to the other catalysts. This indicates that a higher contact time enhances the durability of the catalysts. The absolute values of k_{md}^{250} ($4.6\text{--}10.7 \times 10^{-10} \text{ mol g}^{-1} \text{ Pa}^{-1}$) reported in Fig. 13, although affected to some extent by partial catalyst deactivation, when included into the ranking scale established by Marbán et al. [14] show these catalysts to be among the most active ever synthesized for methanol decomposition.

4. Conclusions

We have demonstrated in this work the feasibility of synthesizing a high surface area $\text{Ni}_{0.7}\text{Zn}_{0.3}\text{O}$ solid solution by means of a room-temperature process, sacrificial template accelerated hydrolysis. The key to achieving this result was the use of a highly polar ZnO template supported on the surface of a stainless steel wire mesh (SSWM), which allowed the material to be produced in a monolithic configuration. The catalyst was produced with a high surface area of around $100 \text{ m}^2 \text{ g}^{-1}$ and in a considerable yield over the SSWM (up to 40 wt.% in the synthesis conditions employed in this work). The characterization of the material by TPR, XRD and XPS revealed that it was composed of an oxygen-defective solid solution with an empirical formula of the type $\text{Zn}^{(2-\sigma)+}_{0.30}\text{Ni}^{(2-\delta)+}[\text{bulk}]_{0.28}\text{Ni}^{2+}[\text{surf}]_{0.25}\text{Ni}^{3+}_{0.17}\text{O}_{1.085-0.15\sigma-0.14\delta}$. The catalyst was not very selective in the methanol steam reforming reaction, as it produced large amounts of CO at temperatures below 400°C . However, at more elevated temperatures the water gas shift reaction improved the hydrogen yield and the carbon selectivity towards CO_2 , especially over higher contact times. Methanol decomposition took place with high conversion degrees and hydrogen yields in the temperature range $250\text{--}350^\circ\text{C}$. In spite of some catalyst deactivation due to coke deposition, which was more noticeable at the highest weight hourly space velocity, this catalyst has been demonstrated to be among the most active catalysts ever reported in the literature.

Acknowledgements

The financial support for this research work provided by the Spanish MEC (CTQ2011-24776) is gratefully acknowledged. Tan T. Vu is grateful to the CSIC for the award of a JAE predoc grant.

References

- [1] A. Navrotsky, A. Muan, J. Inorg. Nucl. Chem. 33 (1971) 35–47.
- [2] H. Kedesdy, A. Drukalsky, J. Am. Chem. Soc. 76 (1954) 5941–5946.
- [3] K.J. Gaskell, A. Starace, M.A. Langell, J. Phys. Chem. C 111 (2007) 13912–13921.
- [4] D. Rodic, V. Spasojevic, V. Kusigerski, R. Tellgren, H. Rundlof, Phys. Status Solidi B: Basic Solid State Phys. 218 (2000) 527–536.
- [5] X. Zhang, K. Kobayashi, Key Eng. Mater. 566 (2013) 191–194.
- [6] F. Rubio-Marcos, C.V. Manzano, J.n.J. Reinos, J.J. Romero, P. Marchet, M.S. Martín-González, J.F. Fernández, J. Phys. Chem. C 115 (2011) 13577–13583.
- [7] J.H. He, C.S. Lao, L.J. Chen, D. Davidovic, Z.L. Wang, J. Am. Chem. Soc. 127 (2005) 16376–16377.
- [8] X.L. Zhang, Y.S. Kang, Inorg. Chem. 45 (2006) 4186–4190.
- [9] X.L. Zhang, R. Qiao, Y. Li, R. Qiu, Y.S. Kang, MRS Online Proc. Libr. 957 (2006) null–null.
- [10] M. El-Hilo, A.A. Dakhel, A.Y. Ali-Mohamed, J. Magn. Mater. 321 (2009) 2279–2283.

- [11] A. Hameed, T. Montini, V. Gombac, P. Fornasiero, *Photochem. Photobiol. Sci.* 8 (2009) 677–682.
- [12] F.T. Lin, N. Li, X.-M. Ma, W.-Z. Shi, *Rengong Jingti Xuebao* 36 (2007) 608–611.
- [13] G. Marbán, I. López, T. Valdés-Solís, A.B. Fuertes, *Int. J. Hydrogen Energy* 33 (2008) 6687–6695.
- [14] G. Marbán, A. López, I. López, T. Valdés-Solís, *Appl. Catal., B: Environ.* 99 (2010) 257–264.
- [15] L. del Río, G. Marbán, *Appl. Catal., B: Environ.* 126 (2012) 39–46.
- [16] T.T. Vu, L. del Río, T. Valdés-Solís, G. Marbán, *J. Hazard. Mater.* 246–247 (2013) 126–134.
- [17] T.T. Vu, L. del Río, T. Valdés-Solís, G. Marbán, *Mater. Res. Bull.* 47 (2012) 1577–1586.
- [18] T.T. Vu, L. del Río, T. Valdés-Solís, G. Marbán, *Appl. Catal., B: Environ.* 140–141 (2013) 189–198.
- [19] T.T. Vu, G. Marbán, *Appl. Catal., B: Environ.* 152–153 (2014) 51–58.
- [20] J. Liu, J. Jiang, M. Bosman, H.J. Fan, *J. Mater. Chem.* 22 (2012) 2419–2426.
- [21] M.-S. Wu, H.-W. Chang, *J. Phys. Chem. C* 117 (2013) 2590–2599.
- [22] M.S. Wilson, *Int. J. Hydrogen Energy* 34 (2009) 2955–2964.
- [23] T. Tsoncheva, V. Mavrodinova, L. Ivanova, M. Dimitrov, S. Stavrev, C. Minchev, *J. Mol. Catal. A: Chem.* 259 (2006) 223–230.
- [24] Y. Matsumura, K. Tanaka, N. Tode, T. Yazawa, M. Haruta, *J. Mol. Catal. A: Chem.* 152 (2000) 157–165.
- [25] J. Xi, Z. Wang, G. Lu, *Appl. Catal., A: Gen.* 225 (2002) 77–86.
- [26] J.H. Jang, Y. Xu, D.H. Chun, M. Demura, D.M. Wee, T. Hirano, *J. Mol. Catal. A: Chem.* 307 (2009) 21–28.
- [27] L. del Río, I. López, G. Marbán, *Appl. Catal., B: Environ.* 150–151 (2014) 370–379.
- [28] N. Kotsev, L. Ilieva, *Catal. Lett.* 18 (1993) 173–176.
- [29] S.R. Kirumakki, B.G. Shpeizer, G.V. Sagar, K.V.R. Chary, A. Clearfield, *J. Catal.* 242 (2006) 319–331.
- [30] R. Moreno-Tost, J. Santamaria-Gonzalez, P. Maireles-Torres, E. Rodriguez-Castellon, A. Jimenez-Lopez, *J. Mater. Chem.* 12 (2002) 3331–3336.
- [31] J.C. Klein, D.M. Hercules, *J. Catal.* 82 (1983) 424–441.
- [32] B.A. Reguig, M. Regragui, M. Morsli, A. Khelil, M. Addou, J.C. Bernède, *Sol. Energy Mater. Sol. Cells* 90 (2006) 1381–1392.
- [33] S. Oswald, W. Brückner, *Surf. Interface Anal.* 36 (2004) 17–22.
- [34] M. Ahmad, E. Ahmed, Z.L. Hong, W. Ahmed, A. Elhissi, N.R. Khalid, *Ultrason. Sonochem.* 21 (2014) 761–773.
- [35] A.P. Grosvenor, M.C. Biesinger, R.S.C. Smart, N.S. McIntyre, *Surf. Sci.* 600 (2006) 1771–1779.
- [36] J.C. de Jesús, P. Pereira, J. Carrazza, F. Zaera, *Surf. Sci.* 369 (1996) 217–230.
- [37] H. Li, H. Liu, J. Wang, S. Yao, X. Cheng, R.I. Boughton, *Mater. Lett.* 58 (2004) 3630–3633.
- [38] K. Remashan, Y.-S. Choi, S.-K. Kang, J.-W. Bae, G.-Y. Yeom, S.-J. Park, J.-H. Jang, *Jpn. J. Appl. Phys.* 49 (2010), 04DF20-01 – 04DF20-07.
- [39] P.K. de Bokx, A.R. Balkenende, J.W. Geus, *J. Catal.* 117 (1989) 467–484.
- [40] D.H. Chun, Y. Xu, M. Demura, K. Kishida, D.M. Wee, T. Hirano, *J. Catal.* 243 (2006) 99–107.